Hollow Fe3O4 spheres as functional architectures for advanced Li–O2 batteries

Journal of Power Sources 684 (2026) 240462

Contents lists available at ScienceDirect

Journal of Power Sources

journal homepage: www.elsevier.com/locate/jpowsour

Hollow Fe_3O_4 spheres as functional architectures for advanced Li–O_2 batteries

Paulina Marquez [a,b], Daniela Alburquenque [c,d], Juan Escrig [e], Carlotta Francia [f], Julia Amici [f,*]

[a] Centro de Investigación en Ingeniería de Materiales (CIIMAT), Universidad Central de Chile, Santa Isabel 1186, Santiago, Chile
[b] Millenium Institute on Green Ammonia as Energy Vector MIGA, ANID/Millenium Science Initiative Program/ICN2021_023, Chile
[c] Center for Applied Nanotechnology, Faculty of Science, Engineering and Technology, Universidad Mayor, Camino La Pirámide 5750, Huechuraba, Santiago, 8580745, Chile
[d] Center for Nanoscience and Nanotechnology (CEDENNA), Avenida Manuel Rodríguez Sur 415, Santiago, Chile
[e] Facultad de Ciencias, Universidad de Santiago de Chile (USACH), Estación Central, Santiago, Chile
[f] Department of Applied Science and Technology (DISAT), Politecnico di Torino, C.so Duca degli Abruzzi 24, Torino, Italy

HIGHLIGHTS

- Fe_3O_4 hollow spheres, prepared through ALD, as ORR catalyst.
- This catalyst is able to shift the ORR from a 2 to a 2 + 2 electrons process.
- In cell, shifting from Li_2O_2 solution growth to surface growth mechanism.
- Enhanced Li_2O_2 reversibility thanks to a reduced crystallinity.
- Reduced DMSO degradation thanks to reduced contact with LiO_2.

GRAPHICAL ABSTRACT

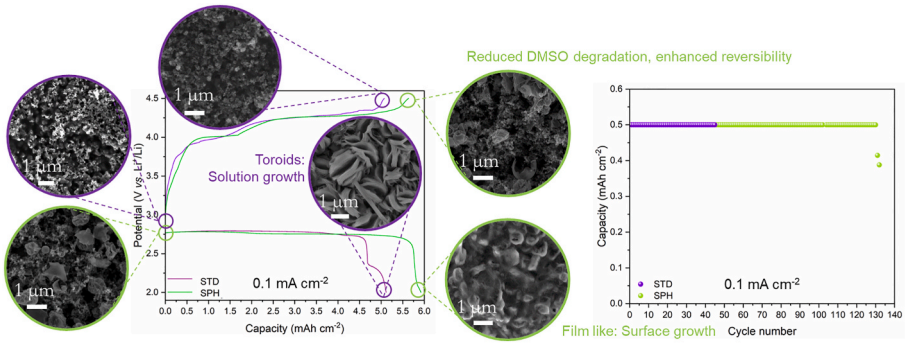

ARTICLE INFO

Keywords:
LiO_2 battery
ORR catalyst
Catalytic activity
Li_2O_2 growth mechanism

ABSTRACT

Although the catalyst intrinsic catalytic activity is crucial for enhancing the performance of Li–O_2 batteries, its morphology also plays a significant role. Bulk catalysts often show limited catalytic efficiency, likely due to their large particle size and low specific surface area. As is well known, highly efficient catalysts require high surface area and a greater number of active sites. In this frame, this work reports the use of Fe_3O_4 hollow spheres obtained through ALD deposition technique onto sacrificial PVP nanoparticles as catalyst for Li–O_2 batteries. Rotating disk electrode studies show the catalyst ability to shift the oxygen reduction reaction (ORR) from a 2 to a 2 + 2 electrons mechanism. Further studies in classical Li–O_2 cell set-up using DMSO with LiTFSI 0.5 M as liquid electrolyte, indicate that the catalyst allows to modify the Li_2O_2 formation pathway upon discharge, from solution to surface growth. This results in higher reversibility and slower DMSO degradation upon cycling visible through a larger full cell capacity (5.9 against 5.1 mAh cm^{-2} for a standard cell), but above all an almost three-

* Corresponding author.
E-mail address: julia.amici@polito.it (J. Amici).

https://doi.org/10.1016/j.jpowsour.2026.240462
Received 20 January 2026; Received in revised form 16 May 2026; Accepted 19 May 2026
Available online 22 May 2026

fold increase of the cycle life (from 45 to 130 cycles, corresponding to approximately 1300 h of operation) at 0.1 mA cm^{-2} and at the curtailed capacity of 0.5 mAh cm^{-2}.

1. Introduction

Rechargeable lithium–oxygen (Li–O_2) batteries have attracted considerable attention as next-generation energy storage systems owing to their exceptionally high theoretical specific energy (≈3500 Wh kg^{-1}) [1], which far exceeds that of conventional lithium-ion batteries [2], as well as other metal-air systems such as Zn-air or Mg-air [3]. Their practical implementation, however, remains severely hindered by sluggish oxygen electrochemistry, electrolyte instability, and poor rechargeability associated with the accumulation of insulating discharge products and, most notably lithium peroxide (Li_2O_2), and related parasitic by-products such as Li_2CO_3 and LiOH [4,5]. These species, formed through complex electrochemical and chemical pathways involving LiO_2 intermediates, progressively passivate the cathode surface, limit charge transport, and trigger electrolyte decomposition, leading to large polarization and poor cycle stability [4–6]. These limitations are closely tied to the oxygen reduction reaction (ORR) during discharge, and the oxygen evolution reaction (OER) during charge, both occurring on the cathode surface and governing the overall reversibility of the system. Charging Li–O_2 batteries in nonaqueous media entails a large overpotential for O_2 evolution, which renders the process highly irreversible and triggers parasitic reactions that compromise both energy efficiency and cycling stability [7]. Understanding and controlling these two coupled reactions are thus crucial to the design of efficient and durable Li–O_2 batteries [1,8]. In nonaqueous Li–O_2 systems, oxygen reduction proceeds through a multistep two-electron pathway. The first electron transfer generates the superoxide anion (O_2^-) at approximately 2.4 V vs. Li^+/Li: $O_2 + e^- \rightarrow O_2^-$ ($E^\circ \approx 2.4$ V vs. Li^+/Li). The O_2^- species then associates with Li^+ to form lithium superoxide: $O_2^- + Li^+ \rightarrow LiO_2$ ($E^\circ \approx 2.3$ V vs. Li^+/Li). The LiO_2 intermediate may either dissolve and disproportionate into lithium peroxide via a solution-mediated mechanism: $2LiO_2 \rightarrow Li_2O_2 + O_2$ ($E^\circ \approx 2.96$ V vs. Li^+/Li) or be directly reduced on the cathode surface to form a conformal Li_2O_2 film (surface growth mechanism). The prevalence of these routes is governed by the solvent donor number (DN), cation–solvent interactions, and the catalytic surface properties [8–10]. In this context, high-DN solvents such as DMSO promote the dissolution and disproportionation of LiO_2, resulting in the formation of large toroidal Li_2O_2 particles through a solution-mediated mechanism. In contrast, catalytic surfaces enriched in oxygen vacancies or transition-metal redox sites favor the direct reduction of O_2 to Li_2O_2 on the surface, leading to nanocrystalline Li_2O_2 films with improved electronic contact and reversibility [9,11]. In aqueous or alkaline electrolytes, the oxygen reduction reaction (ORR) proceeds through either a direct four-electron pathway, $O_2 + 2H_2O + 4e^- \rightarrow 4OH^-$ ($E^\circ = 0.401$ V vs. SHE), or a sequential two-electron route via hydroperoxide intermediates, $O_2 + H_2O + 2e^- \rightarrow HO_2^- + OH^-$ ($E^\circ = -0.065$ V vs. SHE), followed by the further reduction or decomposition of HO_2^-. Unlike the nonaqueous Li–O_2 environment, where the reaction is governed by the formation and accumulation of solid Li_2O_2 and related discharge products, the aqueous ORR is primarily limited by kinetic barriers associated with oxygen adsorption and electron transfer [12,13]. Investigating both regimes, aprotic and alkaline, thus provide complementary insight: the former reveals the thermodynamic and interfacial challenges of Li_2O_2 formation and decomposition, while the latter allows assessment of the intrinsic electrocatalytic activity and kinetics of oxygen reduction and evolution on a given catalyst. The inherent challenges associated with oxygen electrocatalysis, high overpotentials, sluggish reaction kinetics, and electrode passivation by insulating products, have driven intensive research toward the rational design of catalysts capable of promoting both oxygen reduction and evolution reactions. Achieving such bifunctional activity requires a delicate balance between adsorption strength and charge-transfer kinetics for oxygenated intermediates (O_2*, OOH*, O*, and OH*), as well as structural features that facilitate mass transport and maintain electronic connectivity [12,14–16]. Strategies such as defect engineering, modulation of transition-metal oxidation states, and the construction of nanostructured or hollow architectures have proven effective in optimizing these parameters. In this context, transition-metal oxides with mixed valence states and tunable electronic structures have emerged as promising candidates for efficient and durable oxygen electrocatalysis [15,17].

Among transition-metal oxides, magnetite (Fe_3O_4) has gained increasing attention as a redox-active platform for oxygen electrocatalysis. Its intrinsic Fe^{2+}/Fe^{3+} redox couples and moderate electronic conductivity enable efficient oxygen reduction (ORR) activity, while structural tunability and defect engineering can extend its functionality toward the oxygen evolution reaction (OER) [18–21]. Although pristine Fe_3O_4 exhibits limited OER kinetics, compared to mixed-metal oxides, recent studies have shown that introducing oxygen vacancies, FeO-like domains, or heterointerfaces with N-doped carbon significantly enhances bifunctional activity. Such architectures promote the coexistence of surface redox processes ($Fe^{3+}/Fe^{2+} \leftrightarrow Fe^{4+}/Fe^{3+}$) and optimize the balance between intermediate adsorption and oxygen release [15,22]. These findings highlight the potential of Fe_3O_4-based systems as a model framework for rational catalyst design, where controlled surface chemistry and electronic modulation can bridge the activity gap between single-phase oxides and complex bimetallic catalysts. Despite these advances, achieving controlled surface chemistry and defect regulation in Fe_3O_4 remains challenging with conventional wet-chemical synthesis routes. Atomic layer deposition (ALD), with its self-limiting surface reactions, provides a unique opportunity to engineer conformal oxide shells with tunable stoichiometry and defect concentration, enabling precise modulation of catalytic redox sites [23]. It has been extensively used for the growth of metal oxides (e.g., TiO_2, SnO_2, Al_2O_3, and Fe_2O_3) and for tailoring interfaces in energy-related nanostructures [24–27]. One of its key advantages lies in the ability to tune the oxidation state, defect concentration, and morphology of the deposited films by precisely controlling deposition temperature, pulse time, and post-treatment conditions [23].

In a previous work, our group combined electrospraying and ALD to synthesize amorphous Fe_2O_3 coatings on polymer templates, which after calcination yielded crystalline hematite (α-Fe_2O_3) hollow spheres. Subsequent reduction under a H_2/Ar atmosphere transformed these shells into magnetite (Fe_3O_4) with a spinel structure, while preserving the hollow morphology [28]. This controlled amorphous-to-crystalline transition yielded thin-walled hollow structures with a well-defined spinel framework and preserved morphology. Since the conversion of Fe_2O_3 to Fe_3O_4 involves the partial reduction of Fe^{3+} accompanied by oxygen release, it is reasonable to consider that oxygen-deficient sites and structural defects may form during this process, as suggested in previous studies, although no direct evidence is provided in the present work. Consequently, the material exhibits a network rich in Fe^{2+}/Fe^{3+} redox pairs, intrinsic to the magnetite phase, along with defect sites that may act as catalytically active centers during oxygen electrochemical reactions. Such features, including short diffusion paths, high surface area, and electronically active interfaces, make these hollow Fe_3O_4 nanospheres an excellent model to explore the interplay between structural confinement, redox chemistry, and bifunctional oxygen electrocatalysis in Li–O_2 batteries. In this framework, ALD is not merely a coating technique but a rational synthesis tool that allows atomic-scale control of stoichiometry and defect generation, enabling the design of oxide catalysts with optimized redox functionality for next-generation

metal–air systems. The suitability of the prepared hollow spheres as catalyst for Li–O_2 batteries was first studied through rotating disk electrode studies in alkaline aqueous media and then in classical Li–O_2 cell setup, using 0.5 M LiTFSI in DMSO as liquid electrolyte. The performances obtained were systematically compared with those of a cell assembled with an unmodified commercial gas diffusion layer as the cathode. The catalyzed electrode allowed to obtain larger full cell capacity and an almost three-fold increase in the cycle life (with approximately 1300 h of operation), by shifting the discharge mechanism from solution growth to surface growth.

2. Experimental section

2.1. Synthesis of hollow Fe_3O_4 spheres

Polyvinylpyrrolidone (PVP) microspheres were first fabricated by electrospraying a 2 g PVP solution in 10 mL of 50% (v/v) ethanol using a stainless-steel needle (0.9 mm) at 12.9 kV, with a 12 cm tip-to-collector distance, and a feed rate of 0.5 mL h^{-1} for 1 h in a vertical configuration (Spraybase®). The as-prepared PVP spheres were coated with Al_2O_3 by atomic layer deposition (ALD, Savannah S100) to preserve the spherical morphology during subsequent processing. Fifty ALD cycles were carried out at 80 °C, using alternating pulses of trimethylaluminum (TMA, 0.015 s) and H_2O (0.015 s) separated by N_2 purges (30 s and 60 s, respectively). An Fe_2O_3 layer was then deposited by ALD (500 cycles) at 200 °C in stop/exposure mode, using ferrocene ($FeCp_2$) and ozone (O_3, ~10% v/v) as precursors. The $FeCp_2$ source was kept at 80 °C, and each cycle consisted of a 2 s $FeCp_2$ pulse, 5 s exposure, and 15 s evacuation, followed by a 0.2 s O_3 pulse and 15 s purge under a 20 sccm N_2 flow.

After deposition, the PVP/Al_2O_3/Fe_2O_3 composite spheres were calcined in air at 500 °C for 2 h to remove the polymer core and obtain crystalline hematite (α-Fe_2O_3) hollow shells. The resulting hematite spheres were subsequently reduced under a H_2/Ar (5% H_2) flow at 430 °C for 3 h to form magnetite (Fe_3O_4) with a well-defined spinel structure. The Fe_2O_3 to Fe_3O_4 transformation is supported by XRD analysis (Fig. S6), although it should be noted that thermal reduction processes may involve intermediate states or local heterogeneities depending on the reduction conditions. This synthetic route and the corresponding structural and morphological characterization are described in detail in our previous work [28]. The controlled amorphous-to-crystalline transition yielded thin-walled hollow Fe_3O_4 spheres with preserved morphology and a spinel framework featuring the coexistence of Fe^{2+}/Fe^{3+} redox pairs intrinsic to the magnetite phase, which are essential for its redox and electronic properties relevant to oxygen electrocatalysis.

2.2. Electrodes preparation

2.2.1. RRDE electrode preparation for ORR measurements

Oxygen reduction measurements were carried out in 0.1 M KOH prepared with deionized water. Nafion® 5 wt% solution and isopropanol were used for the catalyst ink, consistently with previous procedures [29]. The working ink was formulated by dispersing 5 mg of hollow Fe_3O_4 spheres in 833 μL of deionized water, 167 μL of isopropanol, and 20 μL of Nafion® 5 wt%; the suspension was ultrasonicated for 30 min. A 3 μL aliquot was drop-cast onto the glassy carbon (GC) disk and dried in an oven at 90 °C to form a uniform film, yielding a final catalyst loading of 0.10 mg cm^{-2}.

2.2.2. Electrode preparation for Li–O_2 batteries

The O_2 electrode was prepared as a coating layer over carbon paper gas-diffusion layer (GDL; SIGRACET GDL-39BB, SGL Technologies), consisting of a non-woven carbon paper and a microporous carbon layer, with air permeability equal to 1.5 Gurley s^{-1} according to Sigraget datasheets. To prepare catalyzed cathodes, Fe_3O_4 spheres were mixed with C65 (TIMCAL C-NERGY TM Super C65-Imerys) to ensure good electronic conductivity, and PVDF binder (8 wt%, PVDF in NMP; PVDF from Arkema and NMP from Sigma Aldrich), in a weight ratio of 80:10:10. NMP was added to the mixture to obtain an uniform slurry. The slurry was coated on the top of the microporous layer of the GDL using doctor blade technique. The thickness of the slurry deposited, including the solvent, was set at 100 μm. The obtained electrodes were dried in an oven at 50 °C for 1h and overnight at room temperature before being cut in discs with an area of 2.0 cm^2 and dried again in vacuum at 120 °C for 6 h. The as-prepared cathodes present a Fe_3O_4 spheres loading of 0.32 mg cm^{-2}.

2.3. Physico-chemical characterization

FESEM analysis was carried out by Zeiss SUPRA TM 40 with Gemini column and Schottky field emission tip (tungsten at 1800 K). SEM analysis was carried out through a Zeiss EVO MA10 SEM (Oberkochen, Germany). The size distribution was computed by measuring the diameter of 100 individual particles from SEM images, using ImageJ software. TEM analysis was performed at 120 kV on a Hitachi HT7700 high-resolution TEM (Chiyoda, Tokyo, Japan). HRTEM analysis was performed on a TALOS F200X (Thermo Fisher Scientific, Eindhoven, Netherlands) instrument without aberration correction, operating at an acceleration voltage of 200 kV. Images were captured using a 16-megapixel CMOS camera, and the FFT pattern was processed with Velox software (Thermo Scientific Velox Software, Thermo Fisher Scientific Inc., Waltham, MA,USA). Samples were prepared by dropping dilute suspensions of nanomaterials in ethanol onto carbon film-coated 200 mesh copper grids. XRD analysis was carried out by a PANalytical X'Pert (Cu Ka radiation) diffractometer. Data were collected with a 2D solid state detector (PIXcel) from 10 to 80° with a step size of 0.026° s^{-1}.

2.4. Electrochemical characterization

2.4.1. Electrochemical measurements for ORR in aqueous media

Electrochemical tests were conducted using a PalmSens 4-channel potentiostat/galvanostat coupled to a Japanese RRDE-3A rotator (ver. 3.0). The electrode assembly consisted of a 5 mm glassy carbon disk and a platinum ring, with a rotational range up to 8000 rpm and high stability. A platinum wire was used as the counter electrode, and an Ag/AgCl (sat. KCl) electrode as the reference, connected through a Luggin capillary. The electrolyte (0.1 M KOH) was saturated with either O_2 or Ar for at least 20 min before measurements. Linear sweep voltammetry (RRDE) was performed at a scan rate of 5 mV s^{-1} and a rotation speed of 1600 rpm, while cyclic voltammetry (CV) was recorded between 0.2 and −1.0 V (vs. Ag/AgCl) and LSV was performed from 0.2V to −1.3 V vs. Ag/AgCl. The ring electrode was held at 0.47 V vs. Ag/AgCl (≈1.44 V vs. RHE) to selectively oxidize peroxide species generated at the disk [29]. Potentials are reported vs. RHE using the conversion: $E_{RHE} = E_{Ag/AgCl} + 0.199 + 0.059 \times pH$.

2.4.2. Electrochemical tests for Li–O_2 batteries

For full-cell testing, discs with an area of 2.0 cm^2 were cut from the prepared coated GDL sheets, dried in vacuum at 120 °C for 6 h and used as a cathode. A lithium chip (15.6 mm × 0.62 mm, Chemetall s.r.l.) was used at the anode, a commercial disc of glass fiber (18 × 1.55 mm, ECC1-01-0012-A/L EL-CELL) was used as the separator. 400 μL of the electrolyte solution consisting of LiTFSI 0.5 M in DMSO was added to the cells. The cells were assembled in an Ar-filled glove box (Mbraun Labstar) using an ECC-Air electrochemical cell design (EL-Cell, GmbH). All the results obtained with the cells containing Fe_3O_4 spheres coated GDL (referred to as SPH) were compared to the results obtained with cells assembled exactly in the same way but with bare GDL instead (referred to as STD).

Cyclic voltammetries were performed on STD and SPH cells, on a VSP3-e multichannel potentiostat (Biologic, Seyssinet-Pariset, France), both in oxygen and in argon atmosphere, between 2.0 and 4.5 V vs. Li^+/

Li, at a scan rate of 0.1 mV s^{-1}.

SPH and STD cells were galvanostatically discharged and charged by an Arbin BT-2000 battery tester at room temperature, between 2.0 and 4.5 V vs. Li^+/Li. During measurements, pure O_2 was constantly fluxed at a flow rate of 3.0 mL min^{-1}. Prior to each test, cells rested under oxygen flow for 6 h at open-circuit voltage (OCV).

To get the full discharge/charge capacities of the different cathodes, the cells were galvanostatically discharged at room temperature, from OCV to 2.0 V vs. Li^+/Li at 0.1 mA cm^{-2}, and successively recharged to 4.5 V vs. Li^+/Li. To investigate the cells lifespan, galvanostatic charge and discharge steps were carried out, at the limited capacity of 0.5 mA cm^{-2} at 0.1 mA cm^{-2}, in the voltage range of 2.0–4.5 V vs. Li^+/Li.

3. Results and discussion

3.1. Morphological and structural characterization

As mentioned previously, the magnetite hollow spheres procedure was established by our group in a previous work [28]. Detailed morphological and structural characterizations are reported in the Supporting information. The morphology of the sample was further studied through FESEM and the corresponding micrographs can be seen on Fig. S2, the obtained spheres have quite dispersed size distribution, as reported in Fig. S3. The precursor PVP/Al_2O_3/Fe_2O_3 spheres exhibit an average diameter of 970 ± 213 nm, while the hollow Fe_3O_4 spheres show a reduced average diameter of 685 ± 119 nm, indicating a contraction process during thermal treatment associated with polymer removal and structural rearrangement of the oxide shell.

Moreover, the higher magnification micrographs confirm that the obtained spheres are hollow. The hollow architecture and the presence of partially open and pierced shells are expected to play a key role in facilitating electrolyte penetration and mass transport within the structure. In particular, the existence of sufficiently large internal cavities enables efficient diffusion of reactants and improves accessibility of active sites, which are critical factors during battery operation. TEM analysis was performed to further examine the structure of the hollow Fe_3O_4 spheres. As shown in Fig. S4, the particles exhibit a well-defined hollow morphology, with a clear contrast between the shell and the inner cavity. The shell thickness was estimated to be approximately 15 nm (Figure S4c), consistent with the expected thickness after the ALD process. In addition, HRTEM, carried out on the shells of the spheres (Fig. S5), revealed the presence of fringe lattices, indicating their crystalline nature. While the measured lattice spacings of 0.251, 0.293 and 0.208 nm were found to correspond respectively to the (311), (220) and (400) planes of spinel Fe_3O_4, according to ICSD 01-075-0449.

3.2. ORR activity of hollow Fe_3O_4 spheres in alkaline medium

Cyclic voltammetry (CV) measurements were conducted in O_2-saturated 0.1 M KOH at a scan rate of 10 mV s^{-1}, the corresponding profiles are reported on Fig. 1. It is important to note that, while the alkaline aqueous electrolyte used here differs from the aprotic electrolyte used later in this study, Goodenough et al. [30], as well as other studies, have reported that trends in OER and ORR activity evaluated under alkaline KOH conditions are generally consistent with those observed in organic electrolytes [31,32]. Indeed, Although the alkaline aqueous electrolyte used in RRDE measurements differs from the aprotic electrolyte employed in Li–O_2 batteries, these experiments provide a controlled platform to evaluate the intrinsic oxygen reduction behavior of the catalyst. The insights obtained are used here as a comparative descriptor of catalytic activity, while their relevance to the Li–O_2 system is validated through full cell measurements. Under Ar atmosphere, both the glassy carbon (GC) and Fe_3O_4 hollow spheres electrodes displayed featureless voltammograms, confirming the absence of faradaic processes within the investigated potential range. When the electrolyte was saturated with O_2, a single cathodic peak appeared in both systems, indicating electrocatalytic activity toward the oxygen reduction reaction (ORR).

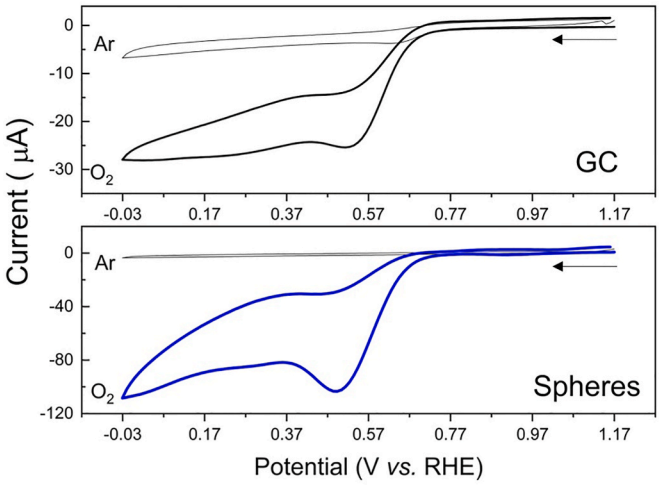

Fig. 1. Cyclic voltammograms in 0.1 M KOH at 10 mV s^{-1} under Ar (grey) and O_2 (Black line) for (top) GC and (Blue line) hollow Fe_3O_4 Spheres. (For interpretation of the references to colour in this figure legend, the reader is referred to the Web version of this article.)

For the GC electrode, the cathodic peak was observed at $E_p = -0.480$ V vs. Ag/AgCl (≈+0.49 V vs. RHE) with a moderate current density. In contrast, the Fe_3O_4 hollow spheres exhibited a broader and more intense reduction signal centered at $E_p = -0.453$ V vs. Ag/AgCl (≈+0.51 V vs. RHE). The higher current density and peak broadening for the hollow spheres suggest enhanced ORR activity, likely associated with their larger electroactive surface area and improved O_2 diffusion through the porous shell structure. This behavior can be attributed not only to the intrinsic catalytic properties of Fe_3O_4 but also to the structural characteristics of the hollow spheres, which provide enhanced mass transport and improved accessibility to electroactive sites.

Although both electrodes show similar reduction potentials, the increased cathodic current observed for the Fe_3O_4 spheres confirms that the material is electrochemically active toward oxygen reduction. However, since only one cathodic feature is resolved within the explored potential window, the detailed reaction pathway (direct four-electron vs. stepwise two-electron process) cannot be determined from these data alone. Therefore, complementary linear sweep and rotating ring–disk electrode (RRDE) studies were conducted to further elucidate the ORR mechanism. The RRDE voltammograms recorded at 5 mV s^{-1} in O_2-saturated 0.1 M KOH for bare glassy carbon (GC) and GC modified with hollow Fe_3O_4 spheres are shown in Fig. 2.

For the GC electrode (Fig. 2a), the disk current displays an onset potential of ≈0.75 V vs. RHE, followed by two diffusion-limited plateaus: a first plateau centered near ~0.50 V vs. RHE and a second extending toward ~0.20 V vs. RHE. Throughout the sweep, the ring current (held at 1.2 V vs. RHE) closely mirrors the disk trace, indicating continuous detection of soluble peroxide species.

For the Fe_3O_4 hollow spheres (Fig. 2b), the disk shows a similar onset at ≈ 0.76 V vs. RHE, again followed by two plateaus: (I) centered at ~0.49 V vs. RHE and (II) extending down to ~ −0.20 V vs. RHE. Compared with GC, the spheres exhibit lower disk currents and a broader reduction wave; notably, the ring current decreases progressively along the cathodic sweep. These differences: broader features, lower disk currents, and a diminishing ring signal for the spheres, suggest a shift from purely diffusional reduction on GC to a surface-mediated process on Fe_3O_4, where Fe^{2+}/Fe^{3+} redox sites facilitate the further reduction of peroxide intermediates.

The observation of two plateaus in both electrodes reflects the

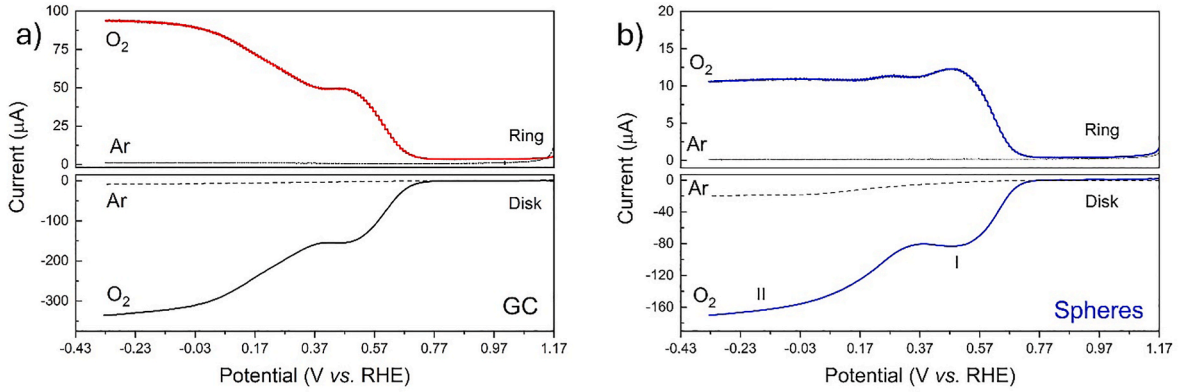

Fig. 2. Rotating ring–disk electrode (RRDE) voltammograms recorded at 5 mV s^{-1} in O_2-saturated 0.1 M KOH of bare GC (a) and GC modified with hollow Fe_3O_4 spheres (b).

sequential reduction of O_2 through soluble peroxide intermediates, within the explored potential window. However, the distinct ring behavior differentiates the two cases: on GC, the ring remains a near mirror image of the disk (indicating that peroxide escapes the disk and is oxidized at the ring), whereas on the Fe_3O_4 spheres, the ring current declines with potential, consistent with further reduction of HO_2^- at the disk. The fact that both systems exhibit a similar E_{onset} indicates that the initial electron transfer to adsorbed O_2 occurs at comparable thermodynamic driving forces on GC and Fe_3O_4. The observed differences, broader features, lower disk currents, and the diminishing ring signal for the spheres, point to modified subsequent kinetics on Fe_3O_4 rather than a shift of the onset itself.

A quantitative assessment of the electron-transfer number and peroxide yield (n and $\%HO_2^-$) is showed in Fig. 3.

The number of electrons transferred (n) and the peroxide yield ($\%HO_2^-$) obtained from RRDE analysis are shown in Fig. 3, for both bare GC and GC modified with hollow Fe_3O_4, spheres. These parameters were calculated from the disk (I_D) and ring (I_R) currents according to standard RRDE equations, using the collection efficiency (N: 0.424) of the setup:

$$n = \frac{4I_D}{I_D + \frac{I_R}{N}} \quad \text{and} \quad \%HO_2^- = \frac{200 \times \frac{I_R}{N}}{I_D + \frac{I_R}{N}}$$

For the bare GC electrode, the oxygen reduction reaction proceeds predominantly through the two-electron pathway, with a peroxide yield above 80% across most of the potential range and an average n value close to 2.3. At the most negative potentials, n shows only a slight increase (e.g., up to ~2.5–2.6) accompanied by a moderate decrease in peroxide yield, suggesting a limited contribution from the further reduction of HO_2^- at the disk surface. This behavior is consistent with the inert nature of GC, which mainly supports the formation and diffusion of soluble peroxide species that are subsequently oxidized at the ring.

In contrast, the Fe_3O_4-modified electrode exhibits a markedly different trend (Fig. 3b). The number of electrons increases from ~3.0 to ~3.5, while the peroxide yield decreases from ~52 % to ~27 % as the potential becomes more cathodic. These results indicate that the hollow magnetite spheres promote the partial conversion of HO_2^- into OH^-, enhancing the overall selectivity toward the four-electron reduction pathway. The inverse relationship between n and $\%HO_2^-$ confirms that Fe_3O_4 catalyzes the subsequent reduction of peroxide intermediates formed during the initial two-electron step.

Comparing both electrodes, it is clear that while GC facilitates oxygen reduction predominantly via the two-electron process, the presence of Fe^{2+}/Fe^{3+} redox sites in the hollow Fe_3O_4 spheres shifts the reaction toward a mixed 2 + 2 electron mechanism, improving selectivity without significantly altering the onset potential. This dual behavior is typical of transition-metal oxides, which can stabilize both adsorbed O_2^- and HO_2^- intermediates and thereby mediate the gradual transformation of peroxide species. It is also important to note that apparent variations in n and $\%HO_2^-$ values can be influenced by film morphology and aggregate structure, since thicker or porous catalytic layers may hinder peroxide diffusion toward the ring and locally affect charge transport. Such effects, previously reported for non-noble metal catalysts in RRDE studies, highlight the relevance of film quality and catalyst dispersion when comparing electrochemical performance [33].

Although the specific intermediates differ between alkaline aqueous and aprotic Li–O_2 media, the sequential 2 + 2 electron process observed

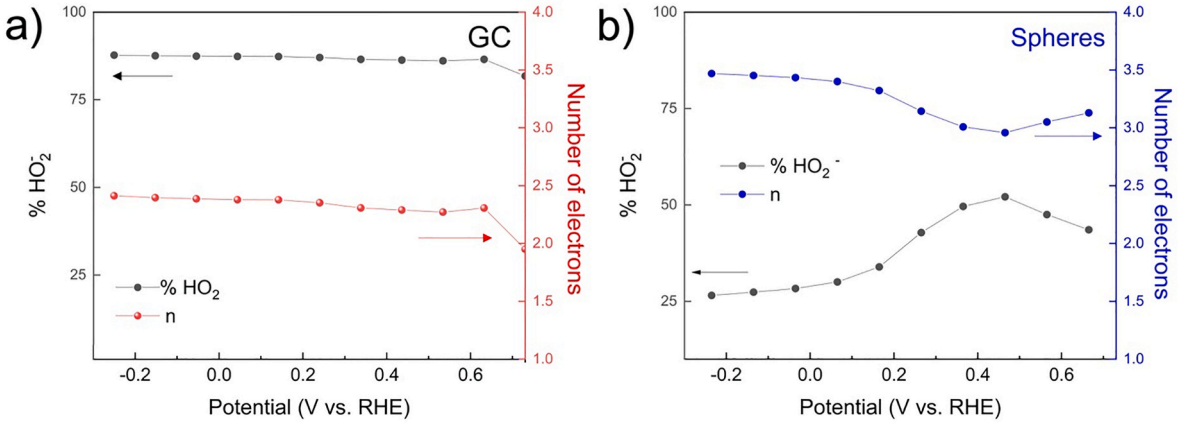

Fig. 3. Calculated peroxide yield ($\%HO_2^-$, left axis) and electron transfer number (n, right axis) obtained from RRDE measurements in 0.1 M KOH at 1600 rpm, with the ring potential held constant. (a) Bare glassy carbon disk; (b) disk modified with hollow Fe_3O_4 spheres.

here illustrates the intrinsic ability of hollow Fe_3O_4 spheres to manage peroxide-type species, a property directly relevant to controlling Li_2O_2 formation and decomposition in Li–O_2 batteries.

3.3. Electrochemical performance of hollow Fe_3O_4 spheres in Li–O_2 batteries

To further confirm these observations air cathodes were prepared by coating a slurry containing the nanospheres, C65 and PVDF onto a commercial gas diffusion layer (GDL39BB) and assembled in a cell together with a glass fiber separator soaked with 0.5 M LiTFSI in DMSO, and a metallic lithium anode (such cells are referred to as SPH). As a means of comparison cells were assembled in the same way but using bare GDL39BB as the cathode (such cells are referred to as STD). Both cells were saturated with O_2 by 4 mL min^{-1} flow for 6 h before performing cyclic voltammetry, the obtained results are reported on Fig. 4.

For both cells a first measurement was carried out in the absence of O_2 to further verify the stability of the cathodic materials against lithium. The obtained voltammograms are perfectly flat in both cases (dotted lines on Fig. 4 a and b) confirming the absence of activity in the potential range investigated. After the cells are saturated with O_2, peaks corresponding to ORR and OER are observed. In particular, the ORR peak of the SPH cell presents a higher current density than the one of the STD cell, at the same time the latter is much wider, which can usually be ascribed to a slower reaction kinetic, and seems to present a shoulder around 2.25 V that would correspond to a second reduction process. Focusing on the ORR onset potential (see Fig. 4 c), it is possible to observe a shift at higher potential for the SPH cell. On the contrary, no particular enhancement is noted for the OER activity, the main difference between the 2 samples is that while the SPH cell presents one main oxidation peak, the STD cell presents three of them that might correspond to the oxidation of degradation products formed during discharge.

To assess cells full capacity and try to elucidate the discharge mechanisms, full discharge tests were carried out at a current density of 0.1 mA cm^{-2}, down to 2 V, both on STD and SPH cells, the corresponding potential profiles are reported on Fig. 5 a and b, respectively. The STD cell reached a capacity of 5.1 mAh cm^{-2}, against 5.9 mAh cm^{-2} for the SPH cell. Interestingly, the discharge profile of the STD cell presents a small second plateau at a potential corresponding to the shoulder noted on the CV profile (Fig. 5 a). Two possible explanations might arise, the first one regards electronic conductivity, indeed if the cathode is covered by insulating Li_2O_2 the electron transfer becomes more and more difficult causing an additional cell polarization [34]. The second explanation would consider the presence of an actual additional reduction process taking place and plausibly resulting in a new discharge product. In order to understand the nature of such discharge products, in both cases the cells were disassembled, and the cathodes were analyzed through FESEM and XRD. The micrographs of the pristine cathodes are reported on Fig. 5 c and d, for the sake of comparison. The STD pristine cathode surface presents the usual morphology of the microporous layer of GDL39BB, while on the surface of the SPH the microspheres are clearly visible and seem to be rather homogeneously distributed. After the discharge process the morphology of both cathodes changes drastically. In the case of the STD cell, the surface is completely covered by micrometric lamellar toroidal structures, completely hiding the microporous layer. On the SPH cell, on the other hand, the surface is completely covered by a homogeneous film, the presence of the microspheres can still be guessed under this film, and no regular micrometric structure is present.

The morphology of Li_2O_2 formed during the ORR process plays a key role in determining its subsequent oxidation behavior and transport properties. Previous studies have shown that different growth mechanisms (surface vs. solution-mediated) lead to distinct Li_2O_2 morphologies, which in turn strongly influence both ionic and electronic transport within the discharge product [35]. In particular, Nazar et al. demonstrated that film-like Li_2O_2 deposition is associated with lower charge overpotentials and improved reversibility, as it promotes more efficient electron transfer across the electrode/electrolyte interface [36]. Moreover, it has been reported that amorphous or poorly crystalline Li_2O_2 exhibits significantly higher ionic conductivity compared to its crystalline counterpart, facilitating Li^+ transport during the charging process [37]. Here, the morphological differences observed between STD and SPH cathodes after cycling (Fig. 5c–f) suggest that the hollow Fe_3O_4 architecture promotes the formation of thinner, more uniformly distributed Li_2O_2 layers on the SPH cathode. This type of morphology is expected to enhance both electron transport (through improved contact with the conductive matrix) and ion transport (through reduced diffusion pathways within the discharge product), thereby facilitating its decomposition during charging. Conversely, the more aggregated or toroidal-like Li_2O_2 structures typically observed on STD cathodes can hinder both electron and ion transport, leading to higher overpotentials and incomplete removal of discharge products.

To further identify the discharge products, the same discharge cathodes were analyzed through XRD, and the corresponding spectra are reported on Fig. 6 a and b. The pristine SPH cathode does not report the peaks characteristic of the Fe_3O_4 spheres, this could be explained first from the low proportion in volume of the spheres compared to the C65 additive, and second by the high crystallinity of the latter, together with GDL, masking the peaks of the former. Focusing on the spectra obtained after discharge, as expected the diffraction pattern of Li_2O_2, the typical discharge product for Li-O_2 system, is visible both on the STD and the SPH cathodes, particularly with the peaks at 32.7°, 34.8° and 58.5°. A second diffraction pattern can be recognized from both spectra, with the most characteristic peaks at 20.4°, 32.5° and 35.7°, corresponding to LiOH, which has been previously associated in literature with DMSO degradation, when in contact with Li_2O_2 and the intermediate of

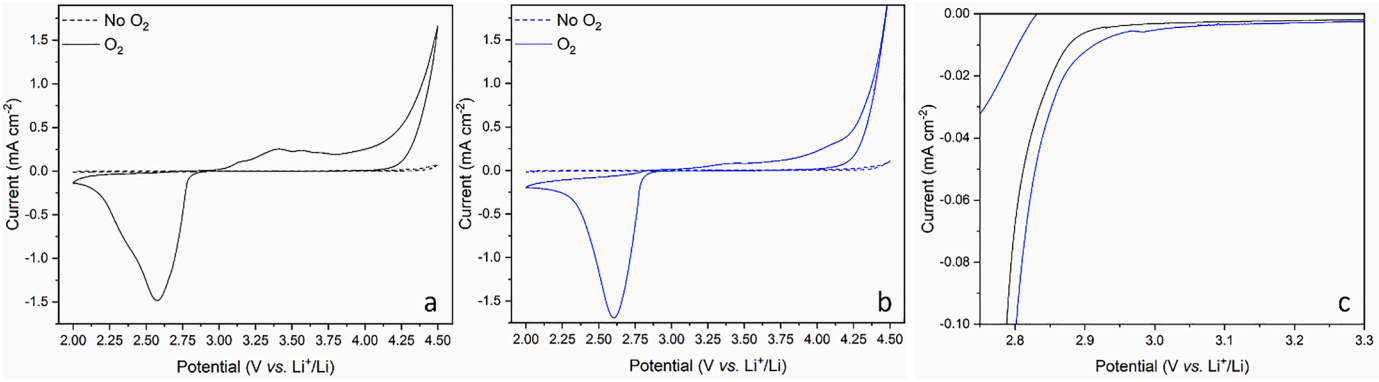

Fig. 4. Cyclic voltammetries performed at 0.1 mV s^{-1} on a STD cell (a) and a SPH cell (b) in presence and absence of O_2. Zoom of the ORR onset region of both voltammograms obtained in O_2 (c).

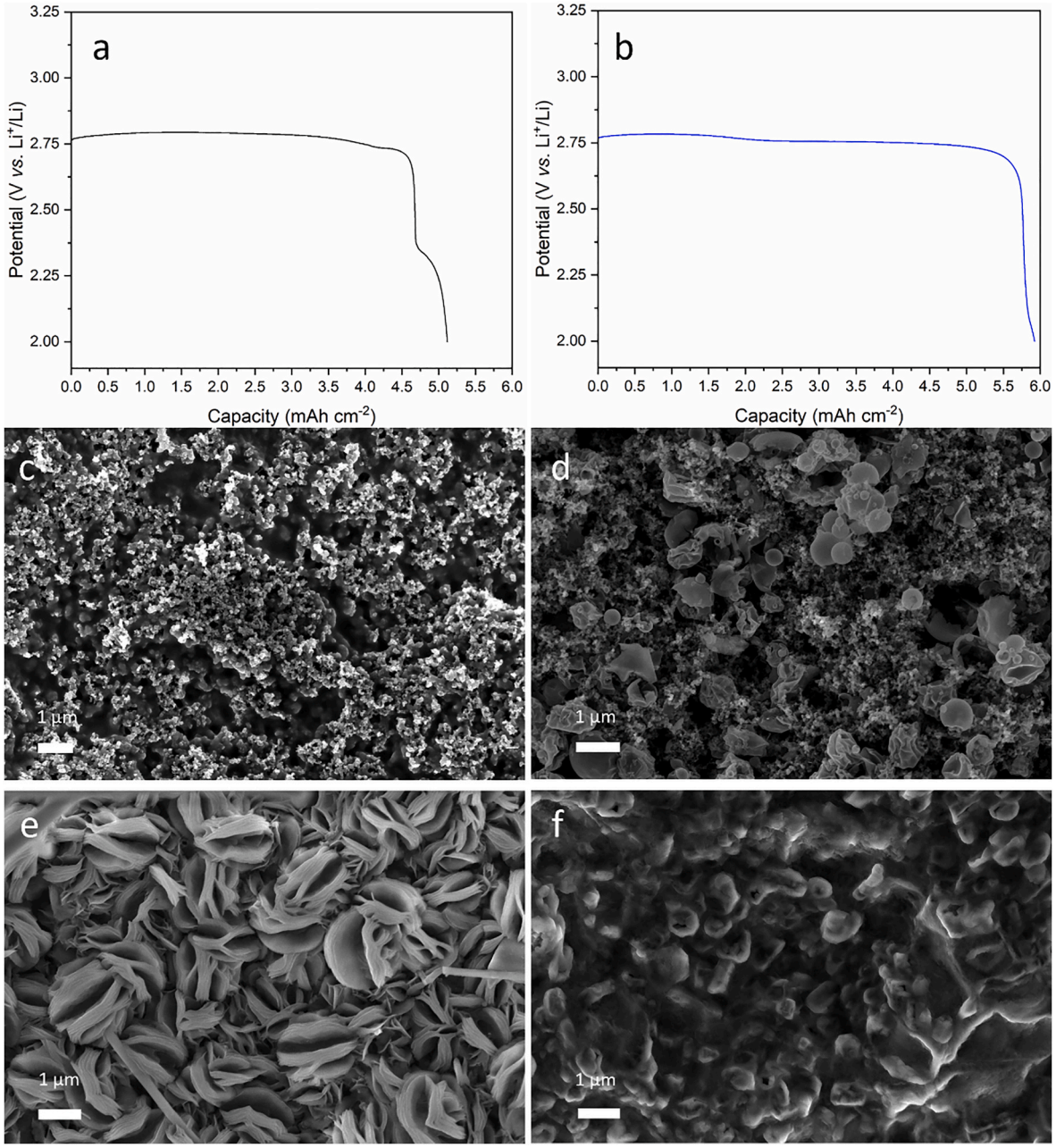

Fig. 5. Full discharge profile of the STD cell (a) and the SPH cell (b) obtained at 0.1 mA cm^{-2} under constant O_2 flow. FESEM micrographs of pristine STD (c) and SPH (d) cathodes and of STD (e) and SPH (f) after full discharge at 0.1 mA cm^{-2}.

reaction LiO_2 [38,39]. For both spectra the peaks intensities were normalized with respect to the main GDL peak (at 26.6°). In these conditions it is possible to note that the intensity of the LiOH peaks, particularly at 32.5° and 37.2° are higher for the STD cell compared to SPH which, keeping in mind that this analysis is not quantitative, should anyway indicate a major presence of this discharge product on the STD cathode.

At this point some hypotheses can be formulated regarding the formation and morphology of the discharge products involved. As widely described in literature [38,40–42], the ORR process, resulting in Li_2O_2 formation, can follow two different pathways, the solution growth and the surface growth, mainly depending on the solvent donor number (DN). The first two steps of ORR are common to both pathways and are the following:

$$O^{*}_{2(g)} + e^{-} \rightarrow O^{-}_{2(sol)} \quad (1)$$

$$Li^{+} + O^{-}_{2(sol)} \rightarrow LiO_2 \quad (2)$$

The dissolved O_2 adsorbed on the cathode surface is reduced to O_2^- (Eq (1)) which reacts with Li^+ solvated in the electrolyte to form the LiO_2 intermediate (Eq (2)).

At this point, DMSO being a solvent with a high DN, and therefore benefiting of a stronger Li^+ solvation [40], the solution growth pathway should occur as follows:

$$LiO_{2(sol)} + LiO_{2(sol)} \rightarrow Li_2O_{2(sol)} + O_2 \quad (3)$$

The previously formed LiO_2 would dissolve in the electrolyte solution and then disproportionate into Li_2O_2 and O_2. (Eq (3)). It has been demonstrated that the solution growth mechanism favors the formation of Li_2O_2 in the form of large toroids or platelets [16,40,41].

On the contrary, in some cases, like with low DN solvents, the formed

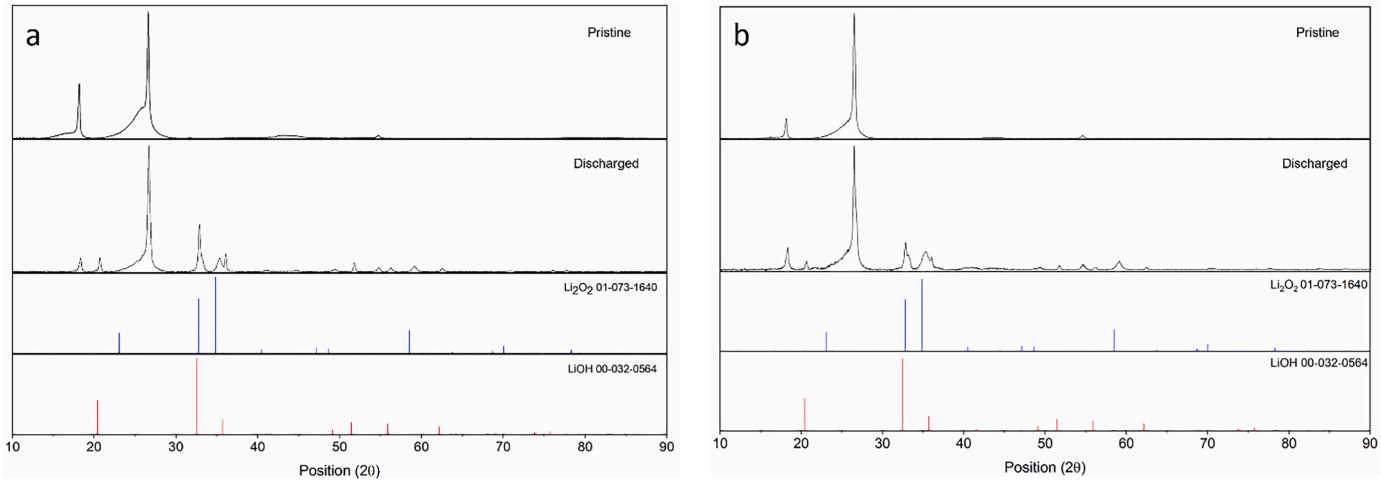

Fig. 6. XRD diffraction patterns for STD (a) and SPH (b) cathodes both pristine and after full discharge.

LiO_2 might be more easily adsorbed on the cathode surface (identified by *), and is therefore exposed to an additional electrochemical reduction to finally form Li_2O_2 (Eq (4)).

$$LiO_2^* + Li^+_{(sol)} \rightarrow Li_2O_2 \quad (4)$$

Through this surface-mediated pathway, Li_2O_2 is usually formed as a thin conformal and nanocrystalline layer on the surface of the cathode [40,41].

Based on the previous results, it is possible to hypothesize that the discharge of the STD cathode occurs through the solution growth pathway, as is to be expected in presence of DMSO, while the SPH cathode experiences the surface growth mechanism. This behavior is consistent with previous studies [18,43], which report that Fe_3O_4 obtained from the partial reduction of Fe_2O_3 may exhibit oxygen-deficient surfaces or defect sites associated with oxygen release during the reduction process. These features have been suggested to promote the nucleation of discharge products and to favor surface-mediated pathways. However, it should be noted that no direct experimental evidence of oxygen vacancies is provided in the present work, and their role is proposed here based on literature reports. This proposed change in the reaction pathway would present two main advantages. First, LiO_2 has strong oxidizing property, therefore its large presence in solution would favor DMSO degradation, detectable from the formation of LiOH during discharge [38,40,41,44]. Second, the formation of Li_2O_2 as a thin film, with much lower crystal size, is easier to decompose thanks to the conformal contact with the cathode surface, which can supply better electron transfer [29,41], as discussed previously.

To assess the reversibility of the discharge products in both cases, after the full discharge, a deep recharge was carried out on both cells, at 0.1 mA cm^{-2} up to 4.5 V. The profiles obtained are reported on Fig. 7a and b.

The STD cell reaches a reversible charge capacity of 5.07 mA cm^{-2} (Fig. 7 a), while the SPH cell reaches 5.63 mAh cm^{-2} (Fig. 7 b), demonstrating in both cases coulombic efficiencies superior to 95%. It is well recognized that LiOH decomposes at potential above 4.3 V [38,44], so by analyzing the recharge curves of both cells, it is possible to assess the proportion of the charge capacity linked, at least in part, to LiOH decomposition. For the STD cell, the potential of 4.3 V is reached when the cell capacity corresponds to 4.09 mAh cm^{-2}, this would mean that all the extra capacity, namely 19.3% of the total charge capacity, is due to LiOH oxidation, together with other possible factors such as cathode pore blockage, incomplete Li_2O_2 decomposition and corrosion of the lithium anode. On the contrary, for the SPH cell the 4.3 V potential corresponds to a cell capacity of 4.74 mAh cm^{-2}, so in this case only 15.8 % of the total charge capacity is due to LiOH, confirming its minor presence and therefore minor electrolyte degradation in the second case, together with a reduced influence of other possible parasitic phenomena.

The discharged cells were disassembled so, once again, the cathodes could be analyzed through XRD and FESEM (see Fig. 7c–f). The obtained XRD spectra of the two recharged cathodes were identical to the ones of the pristine sample (Fig. 7 a and b, upper frames), this complete reversibility was also verified through the FESEM micrographs, which show morphologies similar to the initial ones.

To assess the effect of the microspheres on a longer cycle life, long cycling tests were performed on STD and SPH cells at a limited capacity of 0.5 mAh cm^{-2}, at the current density of 0.1 mA cm^{-2}, the charge-discharge capacity values are reported on Fig. 8 a and b.

The STD cell managed to reach the fixed capacity for 45 cycles while the SPH for 130 cycles, corresponding to approximately 1300 h operation. The end of charge (EoC) and end of discharge (EoD) potentials for each cycle are reported in Fig. 8 c. The STD cell shows an initial decrease in the EoC potential, followed by a steep increase from cycle 13, before reaching the safety cut-off at 4.5 V at cycle 36. This increase can probably be explained by the increasing quantities of LiOH (together with other eventual degradation products) formed at each cycle, necessitating higher and higher overpotential to be decomposed. When the safety cut-off is reached then LiOH and other species cannot be reconverted anymore and they start to accumulate on the cathode surface causing gradual clogging and passivation, thus restraining the charge and mass transfer and increasing the polarization and therefore the EoD potential. Regarding the SPH cell, the increase of the EoC potential is much slower and progressive, reaching the safety cut-off of 4.5 V after 112 cycles. This demonstrates that even if DMSO degradation in Li-O_2 cells is inevitable it can be greatly slowed down by finely tuning the discharge mechanism, for example playing on the catalyst nanostructure, thus enhancing the cycle life.

Last but not least, a careful comparison with recent literature on iron oxide-based catalysts for Li–O_2 cells (Table S1) highlights the competitive performance of the magnetite hollow spheres developed in this work. In particular, while several studies report comparable or even higher initial discharge capacities, these are often obtained under less demanding conditions, such as lower current densities or reduced areal capacities during cycling. In contrast, the present system demonstrates a favorable balance between areal capacity and cycling stability, achieving up to 130 cycles under relatively high current density (0.1 mA cm^{-2}) and fixed capacity (0.5 mAh cm^{-2}), which are more representative of practical operating conditions. Furthermore, many literature reports rely on lower capacity limitations during cycling (typically $\leq$0.4–0.5 mAh cm^{-2}) and/or shorter cycle life (generally

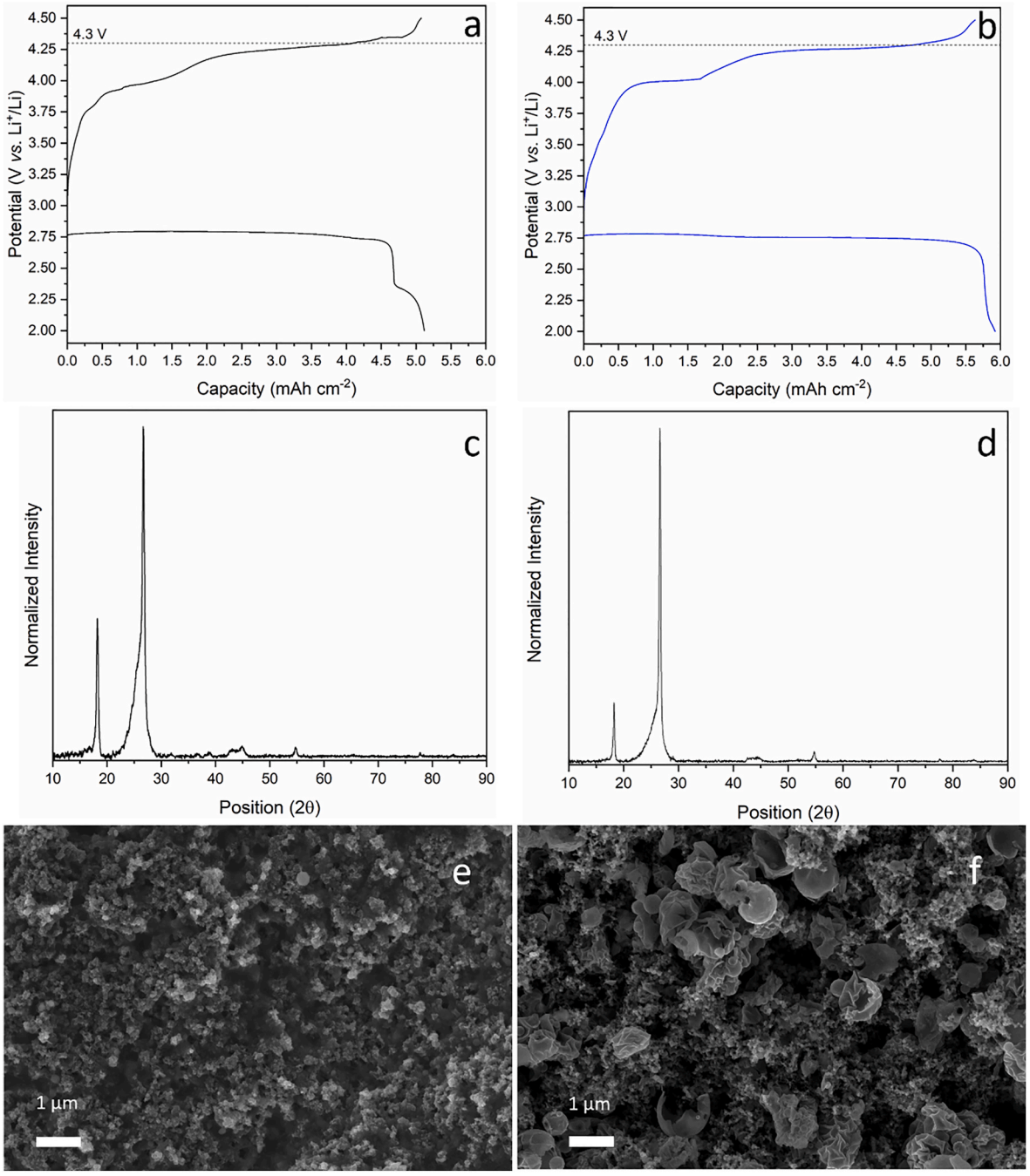

Fig. 7. Full discharge/full charge profiles of STD (a) and SPH (b) cells. XRD diffraction patterns of the fully recharged STD (c) and SPH (d) cathodes. FESEM micrographs of STD (e) and SPH (f) cathodes after full charge.

below 100 cycles), whereas the present work maintains stable operation over an extended number of cycles without compromising capacity. This suggests that the hollow Fe_3O_4 architecture effectively promotes more reversible electrochemical processes and mitigates degradation phenomena. Overall, this comparison indicates that the proposed catalyst provides a well-balanced performance in terms of capacity, stability, and operating conditions, highlighting the beneficial role of the hollow morphology in enhancing both mass transport and reaction reversibility in Li–O_2 systems.

4. Conclusions

This work reports the suitability of Fe_3O_4 hollow spheres, prepared through ALD deposition technique around sacrificial PVP nanoparticles, as catalyst for Li–O_2 batteries. The catalytic activity was first studied through careful rotating disk electrode measurements, carried out in alkaline aqueous media, demonstrating the hollow spheres ability to shift the ORR from a 2 to a 2 + 2 electrons process. Going to an aprotic media in a more classical Li–O_2 cell set up, such hypothesized benefits were verified obtaining larger full cell capacity (5.9 against 5.1 mAh cm^{-2} for an uncatalyzed cathode). More interestingly cathodes post-mortem analyses were consistent with the hypothesis that this catalyst has the ability to shift the Li_2O_2 formation mechanism from the solution growth pathway to the surface growth pathway, thus obtaining smaller and less crystalline discharge products. The benefit of such shifting is two folds, first it allows for a better reversibility of Li_2O_2, second it

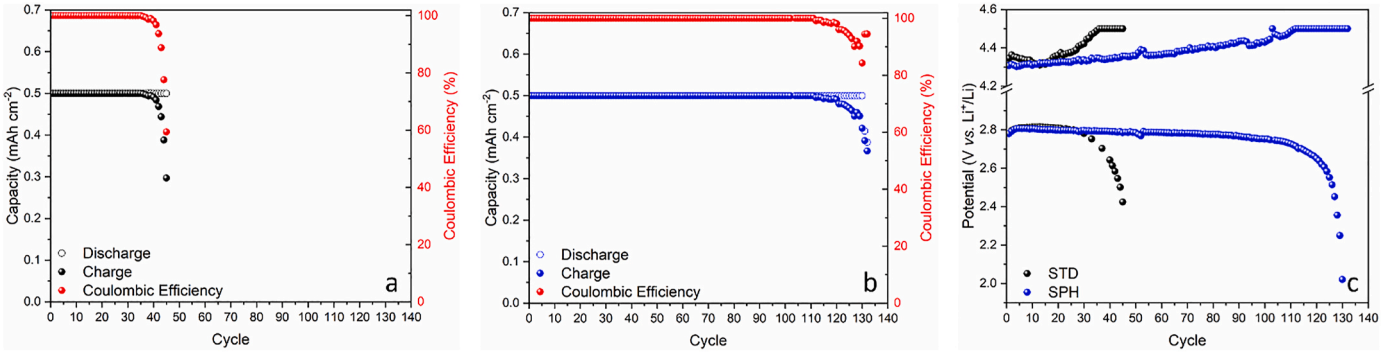

Fig. 8. Long cycling test performed at 0.1 mA cm^{-2}, at a limited capacity of 0.5 mAh cm^{-2}, on STD (a) and SPH (b) cells. Cut-off potential evolution for both cells (c).

diminishes the contact between LiO_2 and DMSO thus probably slowing down the degradation of the latter and the formation and accumulation of LiOH at the cathode surface. These plausible positive effects were further verified through long cycling experiments, comparing the performance of our materials with the one of a cell containing an unmodified GDL layer as the cathode at 0.1 mA cm^{-2} up to the fixed capacity of 0.5 mAh cm^{-2}. It was observed that, not only was the cycle life largely enhanced (from 45 to 130 cycles) but the Fe_3O_4 hollow spheres electrode exhibited a better stabilization of its terminal voltage compared with the standard electrode. As the cycle continues, the gradual clogging and passivation of the electrode by undecomposed discharge products and byproducts restrains the mass and charge transfer and increase polarization in both cases, but in a much slower way for the catalyzed electrode. These results highlight the importance of the hollow architecture in promoting efficient mass transport and reactant accessibility, which contributes to the improved electrochemical performance observed.

CRediT authorship contribution statement

Paulina Marquez: Conceptualization, Data curation, Formal analysis, Funding acquisition, Investigation, Methodology, Supervision, Writing – original draft. **Daniela Alburquenque:** Data curation, Formal analysis, Investigation, Methodology. **Juan Escrig:** Data curation, Formal analysis, Investigation, Methodology. **Carlotta Francia:** Funding acquisition, Writing – review & editing. **Julia Amici:** Conceptualization, Data curation, Formal analysis, Funding acquisition, Investigation, Methodology, Supervision, Writing – original draft.

Declaration of competing interest

The authors declare that they have no known competing financial interests or personal relationships that could have appeared to influence the work reported in this paper.

Acknowledgements

The Authors acknowledge Piano triennale di realizzazione 2025-2027 della ricerca di sistema elettrico nazionale, Progetto integrato: tecnologie di accumulo elettrochimico e termico", PTR 25-27 (MISE ENEA) for the fundings. Millennium Institute on Green Ammonia as Energy Vector - MIGA (ICN2021_023) supported by the Millennium Scientific Initiative of the Ministry of Science, Technology, Knowledge, and Innovation (Chile). Proyecto CIP2023025, Universidad Central de Chile, Proyecto Fondecyt 11230889 y 1240829.

Appendix A. Supplementary data

Supplementary data to this article can be found online at https://doi.org/10.1016/j.jpowsour.2026.240462.

Data availability

Data will be made available on request.

References

[1] P.G. Bruce, S.A. Freunberger, L.J. Hardwick, J.-M. Tarascon, Li–O2 and Li–S batteries with high energy storage, Nat. Mater. 11 (2012) 19–29, https://doi.org/10.1038/nmat3191.
[2] F. Ahmad, A. Arif, M.I. Khan, S. Anjum, A. Shanableh, M.B. Taj, R. Luque, Recent progress and perspectives on lithium and non-lithium rechargeable battery systems, J. Power Sources 648 (2025) 237362, https://doi.org/10.1016/j.jpowsour.2025.237362.
[3] T. Li, M. Huang, X. Bai, Y.-X. Wang, Metal–air batteries: a review on current status and future applications, Prog. Nat. Sci. Mater. Int. 33 (2023) 151–171, https://doi.org/10.1016/j.pnsc.2023.05.007.
[4] S. Karunarathne, C.K. Malaarachchi, A.M. Abdelkader, A.R. Kamali, Advances in bifunctional electrocatalysts towards high-performing Li-air batteries, J. Power Sources 607 (2024) 234553, https://doi.org/10.1016/j.jpowsour.2024.234553.
[5] P. Xing, P. Sanglier, X. Zhang, J. Li, Y. Li, B.-L. Su, Advances in cathode materials for Li-O2 batteries, J. Energy Chem. 95 (2024) 126–167, https://doi.org/10.1016/j.jechem.2024.03.016.
[6] C. Dang, Q. Mu, X. Xie, X. Sun, X. Yang, Y. Zhang, S. Maganti, M. Huang, Q. Jiang, I. Seok, W. Du, C. Hou, Recent progress in cathode catalyst for nonaqueous lithium oxygen batteries: a review, Adv. Compos. Hybrid Mater. 5 (2022) 606–626, https://doi.org/10.1007/s42114-022-00500-8.
[7] B.D. McCloskey, A. Valery, A.C. Luntz, S.R. Gowda, G.M. Wallraff, J.M. Garcia, T. Mori, L.E. Krupp, Combining accurate O 2 and li 2 O 2 assays to separate discharge and charge stability limitations in nonaqueous Li–O 2 batteries, J. Phys. Chem. Lett. 4 (2013) 2989–2993, https://doi.org/10.1021/jz401659f.
[8] W.-J. Kwak Rosy, D. Sharon, C. Xia, H. Kim, L.R. Johnson, P.G. Bruce, L.F. Nazar, Y.-K. Sun, A.A. Frimer, M. Noked, S.A. Freunberger, D. Aurbach, Lithium–Oxygen batteries and related systems: potential, status, and future, Chem. Rev. 120 (2020) 6626–6683, https://doi.org/10.1021/acs.chemrev.9b00609.
[9] N.B. Aetukuri, B.D. McCloskey, J.M. García, L.E. Krupp, V. Viswanathan, A. C. Luntz, Solvating additives drive solution-mediated electrochemistry and enhance toroid growth in non-aqueous Li–O2 batteries, Nat. Chem. 7 (2015) 50–56, https://doi.org/10.1038/nchem.2132.
[10] B.D. McCloskey, C.M. Burke, J.E. Nichols, S.E. Renfrew, Mechanistic insights for the development of Li–O 2 battery materials: addressing Li 2 O 2 conductivity limitations and electrolyte and cathode instabilities, Chem. Commun. 51 (2015) 12701–12715, https://doi.org/10.1039/C5CC04620C.
[11] Y. Wang, Z. Liang, H. Zheng, R. Cao, Recent progress on defect-rich transition metal oxides and their energy-related applications, Chem. Asian J. 15 (2020) 3717–3736, https://doi.org/10.1002/asia.202000925.
[12] X. Ge, A. Sumboja, D. Wuu, T. An, B. Li, F.W.T. Goh, T.S.A. Hor, Y. Zong, Z. Liu, Oxygen reduction in alkaline media: from mechanisms to recent advances of catalysts, ACS Catal. 5 (2015) 4643–4667, https://doi.org/10.1021/acscatal.5b00524.
[13] H. Qiu, S. Wen, Q. Fu, X. Zhao, Oxygen reduction reactions of catalysts with asymmetric atomic structures: mechanisms, applications, and challenges, Catalysts 15 (2025) 615, https://doi.org/10.3390/catal15070615.
[14] K.A. Jannath, H.A. Saputra, Transition metal-based electrocatalysts for alkaline oxygen evolution reaction: developments, challenges, and perspectives, Next Mater. 9 (2025) 101164, https://doi.org/10.1016/j.nxmate.2025.101164.
[15] M.J. Shabdin, W.Y. Wong, K.S. Loh, N.A.F. Othman, H. Yang, M.A. Abdullah, A. Kamal, K.L. Lim, Advances in iron-based electrocatalysts for oxygen evolution in alkaline water splitting: atomic, bimetallic, and high-entropy materials, J. Electroanal. Chem. 996 (2025) 119374, https://doi.org/10.1016/j.jelechem.2025.119374.
[16] S. Martinez Crespiera, D. Amantia, E. Knipping, C. Aucher, L. Aubouy, J. Amici, J. Zeng, C. Francia, S. Bodoardo, Electrospun Pd-doped mesoporous carbon nano fibres as catalysts for rechargeable Li–O 2 batteries, RSC Adv. 6 (2016) 57335–57345, https://doi.org/10.1039/C6RA09721A.

[17] X. Zhao, Z. Hao, X. Zhang, L. Li, Y. Gao, L. Liu, Alkaline oxygen reduction/evolution reaction electrocatalysis: a critical review focus on orbital structure, non-noble metal catalysts, and descriptors, Chem. Eng. J. 497 (2024) 155005, https://doi.org/10.1016/j.cej.2024.155005.
[18] S.I.A. Shah, W. Ahmad, M. Anwar, R. Shah, J.A. Khan, N.S. Shah, A. Al-Anazi, C. Han, Synthesis, properties, and applications of Fe3O4 and Fe3O4-based nanocomposites: a review, Applied Catalysis O: Open 203 (2025) 207049, https://doi.org/10.1016/j.apcato.2025.207049.
[19] K. Kakaei, Y. Aykut, A. Bayrakçeken, Facile synthesis multifaceted Fe3O4 based on N-doped porous carbon frameworks for ORR/OER and study of an external magnetic field, Electrochim. Acta 541 (2025) 147319, https://doi.org/10.1016/j.electacta.2025.147319.
[20] H.-X. Liao, D.-N. Ou, X.-F. Zhou, Y.-Q. Ouyang, H.-H. Jiang, N. Li, Z.-Q. Liu, Static magnetic field-enhanced cathodic electrocatalysis of Fe3O4-based nitrogen-doped carbon for improving the performance of microbial fuel cells, Bioresour. Technol. 426 (2025) 132345, https://doi.org/10.1016/j.biortech.2025.132345.
[21] L. Wang, J. Xiao, Q. Mao, C. Cai, Q. Zhong, C. Liu, M. Liu, Fe3O4 encapsulated in hierarchically porous nitrogen-doped graphitic carbon layers for efficient oxygen reduction reaction: enhanced intrinsic activity via directional interfacial charge transfer, J. Colloid Interface Sci. 679 (2025) 588–599, https://doi.org/10.1016/j.jcis.2024.10.122.
[22] E. Bianchetti, D. Perilli, C. Di Valentin, Improving the oxygen evolution reaction on Fe $_3$ O $_4$ (001) with single-atom catalysts, ACS Catal. 13 (2023) 4811–4823, https://doi.org/10.1021/acscatal.3c00337.
[23] J.A. Oke, T.-C. Jen, Atomic layer deposition and other thin film deposition techniques: from principles to film properties, J. Mater. Res. Technol. 21 (2022) 2481–2514, https://doi.org/10.1016/j.jmrt.2022.10.064.
[24] J. Yang, D. Ma, Y. Li, P. Zhang, H. Mi, L. Deng, L. Sun, X. Ren, Atomic layer deposition of amorphous oxygen-deficient TiO2-x on carbon nanotubes as cathode materials for lithium-air batteries, J. Power Sources 360 (2017) 215–220, https://doi.org/10.1016/j.jpowsour.2017.05.094.
[25] C. Gong, L. Zhao, S. Li, H. Wang, Y. Gong, R. Wang, B. He, Atomic layered deposition iron oxide on perovskite LaNiO3 as an efficient and robust bi-functional catalyst for lithium oxygen batteries, Electrochim. Acta 281 (2018) 338–347, https://doi.org/10.1016/j.electacta.2018.05.161.
[26] J.W. Kim, D.H. Kim, D.Y. Oh, H. Lee, J.H. Kim, J.H. Lee, Y.S. Jung, Surface chemistry of LiNi0.5Mn1.5O4 particles coated by Al2O3 using atomic layer deposition for lithium-ion batteries, J. Power Sources 274 (2015) 1254–1262, https://doi.org/10.1016/j.jpowsour.2014.10.207.
[27] X. Xia, Y. Wang, D. Wang, Y. Zhang, Z. Fan, J. Tu, H. Zhang, H.J. Fan, Atomic-layer-deposited iron oxide on arrays of metal/carbon spheres and their application for electrocatalysis, Nano Energy 20 (2016) 244–253, https://doi.org/10.1016/j.nanoen.2015.12.015.
[28] P. Márquez, C. Patiño Vidal, A. Pereira, L. Vivas, J.L. Palma, C. López de Dicastillo, J. Escrig, Hollow iron oxide nanospheres obtained through a combination of atomic layer deposition and electrospraying technologies, Nanomaterials 12 (2022) 3180, https://doi.org/10.3390/nano12183180.
[29] J. Amici, P. Marquez, A. Mangini, C. Torchio, D. Dessantis, D. Versaci, C. Francia, M.J. Aguirre, S. Bodoardo, Sustainable, economic, and simple preparation of an efficient catalyst for Li-O2 batteries, J. Power Sources 546 (2022) 231942–231953.
[30] Z. Du, P. Yang, L. Wang, Y. Lu, J.B. Goodenough, J. Zhang, D. Zhang, Electrocatalytic performances of LaNi1−Mg O3 perovskite oxides as bi-functional catalysts for lithium air batteries, J. Power Sources 265 (2014) 91–96, https://doi.org/10.1016/j.jpowsour.2014.04.096.
[31] M. Liu, L. Wang, K. Zhao, S. Shi, Q. Shao, L. Zhang, X. Sun, Y. Zhao, J. Zhang, Atomically dispersed metal catalysts for the oxygen reduction reaction: synthesis, characterization, reaction mechanisms and electrochemical energy applications, Energy Environ. Sci. 12 (2019) 2890–2923, https://doi.org/10.1039/C9EE01722D.
[32] Y. Zhao, L. Xu, L. Mai, C. Han, Q. An, X. Xu, X. Liu, Q. Zhang, Hierarchical mesoporous perovskite La 0 .5 Sr 0.5 CoO 2.91 nanowires with ultrahigh capacity for Li-air batteries, Proc. Natl. Acad. Sci. 109 (2012) 19569–19574, https://doi.org/10.1073/pnas.1210315109.
[33] S. Ünsal, T.J. Schmidt, J. Herranz, Effect of aggregate size and film quality on the electrochemical properties of non-noble metal catalysts in rotating ring disk electrode measurements, Electrochim. Acta 445 (2023) 142024, https://doi.org/10.1016/j.electacta.2023.142024.
[34] S.S. Zhang, D. Foster, J. Read, Discharge characteristic of a non-aqueous electrolyte Li/O2 battery, J. Power Sources 195 (2010) 1235–1240, https://doi.org/10.1016/j.jpowsour.2009.08.088.
[35] B.D. Adams, C. Radtke, R. Black, M.L. Trudeau, K. Zaghib, L.F. Nazar, Current density dependence of peroxide formation in the Li–O2 battery and its effect on charge, Energy Environ. Sci. 6 (2013) 1772, https://doi.org/10.1039/c3ee40697k.
[36] D. Kundu, R. Black, E.J. Berg, L.F. Nazar, A highly active nanostructured metallic oxide cathode for aprotic Li–O $_2$ batteries, Energy Environ. Sci. 8 (2015) 1292–1298, https://doi.org/10.1039/C4EE02587C.
[37] F. Tian, M.D. Radin, D.J. Siegel, Enhanced charge transport in amorphous li $_2$ O $_2$, Chem. Mater. 26 (2014) 2952–2959, https://doi.org/10.1021/cm5007372.
[38] D. Sharon, M. Afri, M. Noked, A. Garsuch, A.A. Frimer, D. Aurbach, Oxidation of dimethyl sulfoxide solutions by electrochemical reduction of oxygen, J. Phys. Chem. Lett. 4 (2013) 3115–3119, https://doi.org/10.1021/jz4017188.
[39] S. Yang, P. He, H. Zhou, Research progresses on materials and electrode design towards key challenges of Li-air batteries, Energy Storage Mater. 13 (2018) 29–48, https://doi.org/10.1016/j.ensm.2017.12.020.
[40] F. Wang, X. Li, X. Hao, J. Tan, Review and recent advances in mass transfer in positive electrodes of aprotic Li–O 2 batteries, ACS Appl. Energy Mater. 3 (2020) 2258–2270, https://doi.org/10.1021/acsaem.9b02237.
[41] T. Liu, S. Zhao, Q. Xiong, J. Yu, J. Wang, G. Huang, M. Ni, X. Zhang, Reversible discharge products in Li–Air batteries, Adv. Mater. 35 (2023), https://doi.org/10.1002/adma.202208925.
[42] S.-W. Jee, W. Choi, C.H. Ahn, G. Yang, H.K. Cho, J.-H. Lee, C. Yu, Enhanced oxygen reduction and evolution by in situ decoration of hematite nanoparticles on carbon nanotube cathodes for high-capacity nonaqueous lithium–oxygen batteries, J. Mater. Chem. A Mater. 3 (2015) 13767–13775, https://doi.org/10.1039/C5TA02442K.
[43] X. Li, K. Zhai, C. Fu, H. Huang, C. Liu, M. Xie, C. Zhao, S. Luo, Defect-enriched iron oxide from industrial waste for lithium oxygen batteries with high economic efficiency and industrial feasibility, ACS Sustain. Chem. Eng. 10 (2022) 10493–10502, https://doi.org/10.1021/acssuschemeng.2c01313.
[44] D.G. Kwabi, T.P. Batcho, C.V. Amanchukwu, N. Ortiz-Vitoriano, P. Hammond, C. V. Thompson, Y. Shao-Horn, Chemical instability of dimethyl sulfoxide in lithium–air batteries, J. Phys. Chem. Lett. 5 (2014) 2850–2856, https://doi.org/10.1021/jz5013824.